

# The Zeeman Effect

## Physics 134

Michelle Pichardo Munoz  
University of California at Santa Cruz  
Santa Cruz, CA 95064 USA

June 8, 2022

### Abstract

Excitations due to electrical discharge in gaseous mercury are known to emit unique colors of light or spectra. However, we aim to look deeper into this quantum mechanical phenomenon and incorporate a magnetic field to examine and measure the spectral splitting also known as the Zeeman Effect. We use a Fabry-Perot Interferometer to increase the resolution of our transmitted light to better observe the fine splitting of mercury's green strong line  $\bar{\lambda} = 546.07\text{nm}$ . Based on the theory of electron half integer spin, which came after the initial Zeeman experiment, we expect to find a linear relationship between the splitting and the magnetic field. The slope of our linear fit should be a constant theorized by our experimental set up multiplied by the Bohr Magnetron  $\mu_0$ . In one trial we found the Bohr Magnetron to be  $\bar{\mu}_0 = (8.689 \cdot 10^{-21} \pm 8.091 \cdot 10^{-23}) \text{ erg/Gauss}$  and in the second we found  $\bar{\mu}_0 = (7.250 \cdot 10^{-21} \pm 1.960 \cdot 10^{-22}) \text{ erg/Gauss}$ . These results proved consistent with the expected value  $\mu_0 = 9.2741 \cdot 10^{-21} \text{ erg/Gauss}$  with respective statistical values ( $\chi^2 p = .97$ ) and ( $\chi^2 p = .99$ ).

# Contents

<b>1</b>	<b>Introduction</b>	<b>6</b>
1.1	Physics . . . . .	6
1.1.1	What We Know About Light Emission . . . . .	6
1.1.2	Splitting Due to Spin . . . . .	8
1.1.3	Mercury: Spectral Splitting . . . . .	11
<b>2</b>	<b>Methods</b>	<b>15</b>
2.1	Apparatus . . . . .	15
2.1.1	Mercury Light Source . . . . .	17
2.1.2	Magnetic Field . . . . .	17
2.1.3	Condenser . . . . .	17
2.1.4	Interference Filter . . . . .	17
2.1.5	Polarizer . . . . .	17
2.1.6	Fabry-Perot Interferometer . . . . .	18
2.1.7	Astronomical CCD Camera . . . . .	20
2.2	Measurement . . . . .	21
2.2.1	Calibration Calculation . . . . .	21
2.2.2	Energy Shift Calculation . . . . .	23
2.2.3	Bohr Magnetron $\mu_0$ Calculation . . . . .	24
2.3	Data and Uncertainty Analysis . . . . .	25
2.3.1	Calculation of Uncertainties . . . . .	25
2.3.2	Hypothesis Testing . . . . .	25
<b>3</b>	<b>Results</b>	<b>26</b>
3.1	$\sigma$ Lines . . . . .	27
3.2	$\pi$ Lines . . . . .	28
3.3	$\mu_0$ . . . . .	29
<b>4</b>	<b>Discussion</b>	<b>29</b>
<b>5</b>	<b>Appendix</b>	<b>30</b>
5.1	Data Tables . . . . .	30

# List of Figures

- 1 Two sections examine the properties and transition of a Hydrogen atom. Top: A periodic Table format of Hydrogen showing the atomic number 1 at the top and atomic mass 1.008 amu at the bottom. Next to it is the electron configuration  $[1s^1]$ , where 1 is the energy level  $n = 1$ ,  $s$  is the orbital angular momentum representation of  $\ell = 0$ , and the superscript  $s^1$  represents 1 electron residing in the  $s$ -shell. Bottom: A simplified diagram of an electric dipole transition. #1 contains a neutral atom. The electron and proton effectively cancel each other's effects. #2 Energy was imparted to the atom causing the electron to rise into higher energy. During this brief time, oscillation occurs, causing a nonzero dipole transition ( $\vec{p}$ ) which causes radiation to happen a.k.a light. #3 reveals the photon emitted at a frequency equal to the energy difference (Harris, 2014). . . . . 7
- 2 An electron is under the influence of a weak magnetic field. The moving charge exhibits specific momenta vectors ( $\vec{L}, \vec{S}$ ) and magnetic moments ( $\mu_L, \mu_s$ ), which have a direct dependence on the momenta. The vectors  $\vec{L}$  and  $\vec{S}$  are shown fixed at an angle  $\theta$  while their sum  $\vec{J}$  processes slowly about  $B_{ext}$ . On the opposite end, we find the moments such that the sum  $\mu_J$ , which is not directly opposite to  $\vec{J}$ , is rapidly processing about  $\vec{J}$ . The value  $\mu_{Javg}$ , which is the average value of twirls, is used as a basis for the derivation of our orientation energy of the magnetic dipole transition ( $\delta E$ ). Note that the only definite quantities are the  $z$ -components the vectors shown are extrapolated predictions (Harris, 2014). . . . . 10
- 3 The energy levels for the  $^3S_1 \Rightarrow ^3P_2$  transition in mercury. The left-most green arrow is our electric dipole transition, while the 9 blue, green, and purple arrows are the magnetic dipole transitions. The 9 transitions are identified by their  $m_j$  value and their orientation energy  $\delta E$ . The restrictions categorize these transitions into  $\pi$  and  $\sigma$  lines. The  $x$ -axis represents the relative spacing between energies (Ucsc, 2022) . . . . . 13
- 4 Relative intensities of the Zeeman lines. This is our theoretical model of what we expect to see in our data. The  $\pi$  lines (yellow) appear parallel to  $B_{ext}$  while the  $\sigma$  lines (blue) are perpendicular. The  $x$ -axis is the same as in Figure. 3. The  $\sigma$  lines will not resolve as they are too closely spaced, but the resulting peaks correlate to the line's center of mass (Ucsc, 2022). . . . . 13
- 5 Image of the full optical line. Rays travel from left to right. Mercury Geissler Tube (blue highlight), Hall Probe (purple highlight), Horseshoe Magnet, Condenser, Filter, Interferometer, Polarizer, Aperture, and the CCD Camera. Images from the CCD camera are processed by its associated software where exposure time and other qualities are adjusted. . . . . 16

6	Image of optical setup taken from a different angle to better see the polarizer dial and camera. Rays incoming from left to right. Filter, Interferometer, Polarizer, Aperture, and the CCD Camera. . . . .	16
7	Ray diagram of the Fabry-Perot Interferometer. Top: Rays are incoming from the source light and reflected within the two flats. The reflected ray is green, and it branches away from the blue ray. The red highlighted portion is the extra distance taken by the green ray, which needs to be an integer multiple of the wavelength of our incoming ray to interfere constructively. More on this is found in the Appendix (Ucsc, 2022) . . . . .	19
8	An oversimplified ray diagram of our CCD Camera. Rays are incoming from right to left at a field dimension angle $\theta$ . The lens is set to focus at infinity to produce the sharpest rings (Ucsc, 2022). . . . .	20
9	Image taken from CCD of Mercury's interference pattern. The bright/thick center ring is an example of $p=1$ . Faint white rings appear to crossover Mercury's rings that were not accounted for in the results. . . . .	21
10	Intensity profile of $B_{ext} = 0.001\text{kG}$ . The large vertical lines correlate to the cross-section of bright white rings of Figure. 9. . . . .	21
11	Fit graph for calibration Equation 6. The polarizer was set to 90 degrees during collection. The magnetic field was not zero even though the magnet was turned off $0.001\text{kG}$ was the reading. The calibration was a success with a $p\text{-value} = .78$ . . .	22
12	Peak selection from intensity profiles [ADU vs. Pixel]. Top: $\pi$ profile with $p = 1$ ring. Peaks are selected about the central line, labeled with red (x)'s. Bottom: $\sigma$ profile with $p = 1$ ring. Peaks were also selected about the central line. Values $D_1$ and $D_2$ are the diameters of the respective rings. The relative difference in our selected peaks is labeled with $A$ (Ucsc, 2022) . . . . .	23
13	Mercury's $p=1$ ring intensity profile. This graph is a truncated version of Figure .10. Note that the ring values are located approximately at pixel values 290 and 460. . . . .	26
14	$\sigma$ line splitting observed at $B = 1.401\text{kG}$ . The relative locations of the peaks are similar to Figure .13. The peaks are not fine points and attribute error of $\pm 2$ pixels for narrower peaks and $\pm 3.5$ pixels for wider ones. . . . .	26
15	$\pi$ line splitting observed at $B = 5.800\text{kG}$ . The relative locations of the peaks are similar to Figure .13. The peaks are not fine points and attribute error of $\pm 2$ pixels for narrower peaks and $\pm 3.5$ pixels for wider ones. . . . .	26
16	Fit Graph for $\sigma$ lines taken at 180 degrees. The fitting function is shown above the graph with the value $A = 2.5$ fixed. The best fit values are shown on the plot and in Table 1. . . . .	27

17	Fit Graph for $\pi$ lines taken at 90 degrees. The fitting function is shown above the graph with the value $A = 1$ fixed. The best fit values are shown on the plot and in Table 2 . . . . .	28
----	---	----

## List of Tables

1	Fitted Values from $\sigma$ Trials. . . . .	27
2	Fitted Values from $\pi$ Trials. . . . .	28
3	Table of $\Delta E_i$ and $B$ values for both $\sigma$ and $\pi$ lines. Values are taken from $p = 1$ rings. Values are calculated from our measured diameters and the uncertainty from our peak pixel selection is propagated with an average error of $\pm 2.75$ pixels. . . . .	30
4	Table of $\mu_0$ and $\sigma_{\mu_0}$ values for both $\sigma$ and $\pi$ lines. Their weighted averaged values are $(8.689 \cdot 10^{-21} \pm 8.091 \cdot 10^{-23})$ and $(7.250 \cdot 10^{-21} \pm 1.960 \cdot 10^{-22})$ respectively. Equation to reference: Equation 15 found in section 2.2.3. . . . .	30
5	Fitted values for our calibration test using Equation 6. . . . .	31

# 1 Introduction

For those of us new to the subject of light, it may not be intuitive to say it has a relationship to magnetism. In fact, before 1896, the search for a relationship was unsuccessful. Michael Faraday, known for his work in electricity and magnetism, attempted to find a direct connection between magnetism and a light source by measuring the light with a spectroscope (Perepelista, 2007). He failed to find any conclusive information. However, his work prompted Pieter Zeeman's experiment, which proved successful (Zeeman, 1902). Zeeman was the first to observe the splitting of sodium D-lines under the influence of a magnetic field, where D refers to the yellow strong line of sodium (A J Kox, 1997). Although, at the time of the experiment, the theory to back it was still undetermined. Until 1892, Hendrick Anton Lorentz presented his electron theory to explain Zeeman's discovery (Zeeman, 1902). It is important to note that Lorentz's electron theory came before the discovery of the electron, which was measured in 1913 by Robert Millikan. The years prior to 1892 contained many different interpretations of the inner workings of atoms and their relationship to light which is highly dependent on the speculative topic of electrons and their quantum mechanical properties. For this reason, we set out to perform our experiment and witness the Zeeman effect for ourselves. Our goal is to use this new theory, replicate the Zeeman effect in mercury, and measure the Bohr Magnetron  $\mu_0$ , which is a constant resulting from the theory.

We will discuss the electron theory concerning our experiment in the following sections. We emphasized the electron's intrinsic properties and how they allow us to predict mercury's green strong line splitting. Additionally, we cover the equipment involved and data acquisition.

## 1.1 Physics

The following is an brief account of the theory we will use as factual, the theory we will be testing, and how it relates to our target substance mercury.

### 1.1.1 What We Know About Light Emission

To understand light, we summarize the known governing properties and theories. First, the quantum mechanical wave function  $\Psi_{n,\ell,m_\ell}$  describes an atom's electrons. The mathematical model,  $\Psi_{n,\ell,m_\ell}$ , represents the probability distribution of the electron and contains information on its most probable location in space and its energy (Harris, 2014). Each electron is also associated with a specific set of quantum numbers  $n$ ,  $\ell$ , and  $m_\ell$ .  $n$  is the associate energy level,  $\ell$  is the orbital angular momentum number, and  $m_\ell$  is the magnetic quantum number. More specifically, in the shell-theory, the shell  $n$  is divided into subshells of  $\ell = n - 1$ , and finally, those subshells are divided again into their orientation-specific shells by  $m_\ell = [-\ell, \dots, +\ell]$ . We mention the shell theory because it is helpful to consider an excitation of one electron as "jumping" up to a higher

energy shell or transitioning for a short time and then returning to its favored lower energy while emitting a photon in the process. See the "Shell Model" in **Figure. 1**.

We consider Hydrogen's simple one electron-proton pair configuration to understand the transition better. The theory assumes an excited electron acts as an oscillating electric dipole with its proton counterpart, but only if we meet angular momentum conservation conditions. These conditions are highly dependent on the properties of the photon, which are explained in the following section. Assuming we impart the precise energy to cause an excitation, the electron-proton pair will oscillate at a frequency equal to the emitted light.

This simplified idea extends to more complex atoms because of a property called shielding. Consider our target atom mercury which has 80 electrons ( $e^-$ ) and 80 protons( $e^+$ ). In its non-excited state, the electron-proton pairs effectively cancel out, leaving a neutral atom. However, an atom typically experiences excitations in its outermost shell which only ever holds at most two electrons. When excitation occurs, it will act similarly to the Hydrogen's electron-proton electric dipole transition. More on mercury's transition is seen in the following sections.

To summarize, the following figure is provided as an illustration. The following page contains relevant equations.

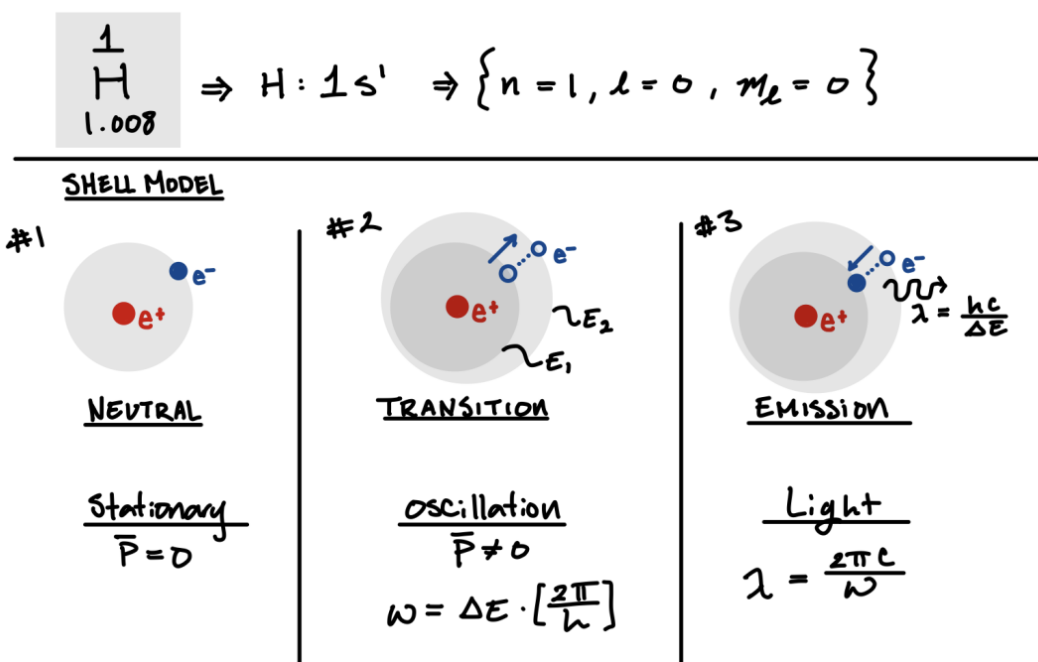


**Figure 1:** Two sections examine the properties and transition of a Hydrogen atom. Top: A Periodic Table format of Hydrogen showing the atomic number 1 at the top and atomic mass 1.008 amu at the bottom. Next to it is the electron configuration  $[1s^1]$ , where 1 is the energy level  $n = 1$ , s is the orbital angular momentum representation of  $\ell = 0$ , and the superscript  $s^1$  represents 1 electron residing in the s-shell. Bottom: A simplified diagram of an electric dipole transition. #1 contains a neutral atom. The electron and proton effectively cancel each other's effects. #2 Energy was imparted to the atom causing the electron to rise into higher energy. During this brief time, oscillation occurs, causing a nonzero dipole transition ( $\vec{p}$ ) which causes radiation to happen a.k.a light. #3 reveals the photon emitted at a frequency equal to the energy difference (Harris, 2014).

Equations of relevance:

Energy of a Photon

$$\Delta E = h(2\pi\omega) = \frac{hc}{\lambda}$$

Electric Dipole

$$\vec{p} = \int_{\text{all space}} (-e\vec{r}) |\vec{\Psi}(\vec{r}, t)|^2 dV$$

$$\vec{p} = -eRe \left( e^{i2\pi\Delta Et/h} \int_{\text{all space}} \vec{r} \psi_2^*(\vec{r}) \psi_1(\vec{r}) dV \right)$$

Where  $h = 6.6262 \cdot 10^{-27}$  erg-sec is Plank's constant,  $c = 2.998 \cdot 10^{10}$  cm/s is the speed of light,  $\lambda$  is the wavelength associated with energy  $\Delta E$ ,  $e = 4.803 \cdot 10^{-10}$  esu is the fundamental charge unit, and  $\vec{r}$  is the position of the electron relative to its proton.

The equation for the electric dipole is taken from Randy Harris's book *Modern Physics* (2014) from the Allowed Transitions section. In summary, this section states that the only instance where  $\vec{p}$  is nonzero is when the wave function  $\Psi$  which depends on  $\ell$  is composed of a transitioned states that follow specific transition rules  $\Delta\ell = \pm 1$  and  $\Delta m_\ell = 0, \pm 1$ .

### 1.1.2 Splitting Due to Spin

As previously mentioned, the electric dipole transitions are heavily dependent on the properties of the photon. To understand this, we must incorporate the next quantum number spin ( $s$ ). Spin is the intrinsic magnetic angular momentum number. We can distinguish electrons from photons by their spin value;  $s = 1/2$  for electrons and  $s = 1$  for photons. The concept of spin is difficult to understand, so let us consider this poor attempt on my part. Feel free to skip this paragraph.

Consider two marbles of different sizes and colors in a Zen sand garden. Imagine that the marbles can create an image in the sand, provided we impart some initial velocity. Say the first marble outlines a circle in the sand while the second outlines an ellipse. At first glance, we could fabricate some relation to the shape it outlined to the physical properties we can see. This, I will say, is analogous to  $\ell$  the orbital angular momenta which gives orientation information. Next, consider something even more outlandish. Say we place the marbles square in the center of the Zen garden, imparting no initial velocity. Suddenly the outlines return -a circle for the first marble and an ellipse for the second. I attribute this to  $s$  the intrinsic angular momenta, which is still capable of interaction with the outside world much like  $\ell$ . However, we cannot interact with  $s$  in the same way we could interact with the marble itself to change  $\ell$ . This example may



have served no purpose, but I was fixated, and here it stands.

As  $s$  and  $\ell$  are both momenta quantities they both have similar conditions in their quantum numbers  $m_s = [-s, \dots, +s]$  and  $m_\ell = [-\ell, \dots, +\ell]$ . Returning to the transition rules we can now observe the photon dependence. Since the conditions are  $\Delta\ell = \pm 1$  and  $\Delta m_\ell = 0, \pm 1$ , the change in orbital momenta  $\ell$  is converted into the intrinsic momenta of the photon upon creation.

With this in mind, we can transition to the theory we are setting out to test. We already covered oscillating electric dipole transitions, but since the electron is not stationary, it is reasonable to assume a magnetic dipole transition could also occur. The proof is a bit involved but can be located in Randy Harris's book *Modern Physics* (2014), Chapter 8: Spin and Atomic Physics.

To summarize, a moving charged particle exhibits a magnetic moment that can be used to find its orientation energy. This energy results from several restrictions placed on the momenta of the particles, which we will see in the following section. However, we can only measure one dimension of our momenta which by convention is the z-axis. We mention this because up until now, all the values were assumed known, and we did not want to make any claim that would violate the uncertainty principle. In any case, the equations are presented along with **Figure. 2** which gives a visual of the electrons momenta. Note,  $m_e$  is not a quantum number but the mass of the electron.

#### Momenta: Magnitudes & Quantum numbers

$$\begin{aligned}
 |\vec{L}| &= \sqrt{\ell(\ell+1)}\hbar & m_\ell &= [-\ell, \dots, \ell] & n &> 0 \\
 |\vec{S}| &= \sqrt{s(s+1)}\hbar & m_s &= [-s, \dots, s] & \ell &= n-1 \\
 \vec{J} &= \vec{L} + \vec{S} & m_j &= [-j, \dots, j] & s &= (e^- : 1/2, \text{Photon} : 1) \\
 |\vec{J}| &= \sqrt{j(j+1)}\hbar & j &= |\ell - s|, \dots, (\ell + s) .
 \end{aligned} \tag{1}$$

As a consequence we have new restrictions:  $\Delta m_s = 0$  and  $\Delta m_j = 0, \pm 1$

#### Magnetic Moments:

Both physical and intrinsic momenta contribute their unique moment.

$$\begin{aligned}
 \vec{\mu}_L &= -\frac{e}{2m_e}\vec{L} & \vec{\mu}_S &= -\frac{e}{m_e}\vec{S} \\
 \vec{\mu}_J &= \vec{\mu}_L + \vec{\mu}_S = -\frac{e}{2m_e}(\vec{L} + 2\vec{S})
 \end{aligned}$$

Orientation Energy as a function of  $m_j$ , an external magnetic field  $B_{ext}$ , and the Bohr Magnetron  $\mu_0$ . The equation is derived from the image below and the  $\mu_{Javg}$ .

$$U = \delta E = g_{Lande} \cdot \left( \frac{e}{2m_e} \cdot \hbar \right) \cdot m_j \cdot B_{ext} \quad (2)$$

$$= g_{Lande} \cdot (\mu_0) \cdot m_j B_{ext}$$

$$g_{Lande} = 1 + \frac{j(j+1) + s(s+1) - \ell(\ell+1)}{2j(j+1)} \quad (3)$$

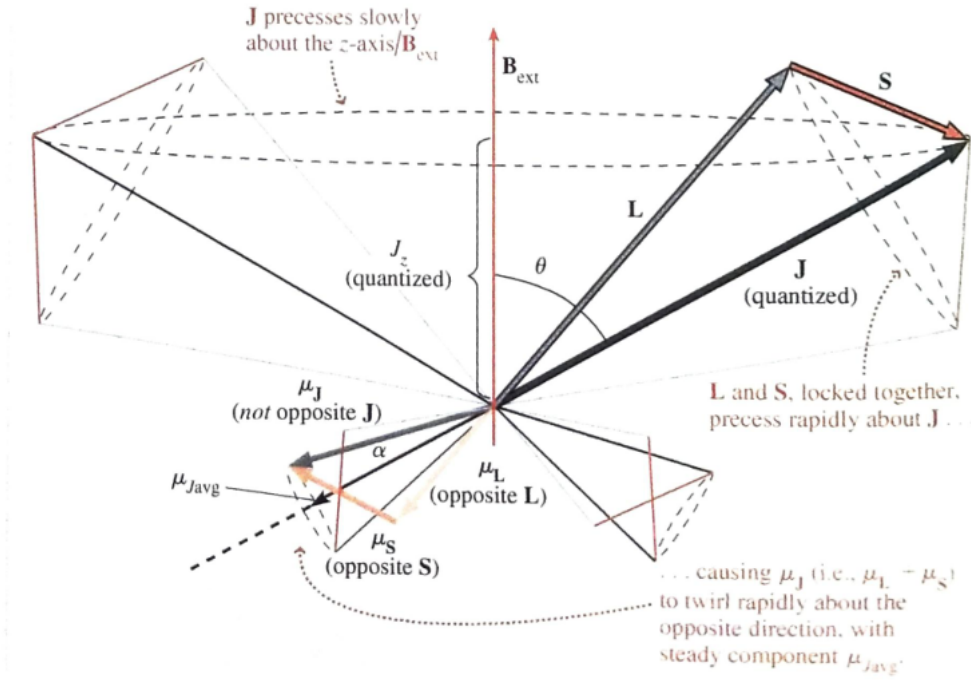


**Figure 2:** An electron is under the influence of a weak magnetic field. The moving charge exhibits specific momenta vectors ( $\vec{L}, \vec{S}$ ) and magnetic moments ( $\mu_L, \mu_s$ ), which have a direct dependence on the momenta. The vectors  $\vec{L}$  and  $\vec{S}$  are shown fixed at an angle  $\theta$  while their sum  $\vec{J}$  processes slowly about  $B_{ext}$ . On the opposite end, we find the moments such that the sum  $\mu_J$ , which is not directly opposite to  $\vec{J}$ , is rapidly processing about  $\vec{J}$ . The value  $\mu_{Javg}$ , which is the average value of twirls, is used as a basis for the derivation of our orientation energy of the magnetic dipole transition ( $\delta E$ ). Note that the only definite quantities are the z-components the vectors shown are extrapolated predictions (Harris, 2014).

### 1.1.3 Mercury: Spectral Splitting

Using gaseous mercury we apply all of the previous theory.

Shell Model: Electron Configuration of Mercury Hg

$$\text{Hg} : [\text{Xe}]4f^{14}5d^{10}6s^2$$

Where [Xe] is short for the remaining 54 electrons in the lower energy shells, and letters f, d, and s represent  $\ell = 3, 2, 0$  respectively. This is the neutral state of Mercury, and all 80 electrons cancel with all 80 protons. We are interested in the excitation of the two electrons within the outermost 6s shell. The excitation and de-excitation steps are as follows.

$$(6s^2) = (6s^1)(6s^1) \longrightarrow (6s^1)(7s^1) \implies (6s^1)(6p^1) \longrightarrow (6s^1)(6s^1)$$

We see the outermost electron will excite up to the 7s shell, then de-excite to the 6p ( $\ell = 1$ ) shell, then de-excite once more to its neutral state. Our interest lies with,

$$(6s^1)(7s^1) \implies (6s^1)(6p^1)$$

We have not covered the multi-particle aspect of these transitions. So now, we examine each electron in its respective shell and apply our momenta equations.

$$\begin{aligned} 6s^1 : \ell &= 0 & s &= 1/2 \\ 7s^1 : \ell &= 0 & s &= 1/2 \\ \ell_T &= 0 & s_T &= 0, 1 \\ j_T &= 0, 1 \\ m_{j_T} &= [-1, 0, 1] \end{aligned}$$

Where  $\ell_T, s_T$ , and  $j_T$  are the sum momenta values of the two electrons. Note, the two electrons can only have  $s_T$  values of either 0 for anti-aligned or 1 for aligned. The totals in this excitation state ( $6s^1 7s^1$ ) give two possible combinations, which we refer to as terms and use a new notation, where  $\chi$  is the letter representation of  $\ell_T$ .

$$\text{Term}_{s_T, \ell_T, j_T} = {}^{2s_T+1}[\chi]_{j_T}$$

$$(s_T, \ell_T, j_T) = (0, 0, 0), (1, 0, 1) = {}^1S_0, {}^3S_1$$

A similar approach is taken for the state ( $6s^1 6p^1$ ). The resulting terms are,

$$^1P_1, \quad ^3P_0, \quad ^3P_1, \quad ^3P_2$$

The electron has up to 8 possible transitions from our excited state, each with a unique characteristic wavelength (UCSC, 2022). However, in our experiment, we are only interested in the electric dipole transition,

$$^3S_1 \implies ^3P_2$$

which results in the bright green line at  $\bar{\lambda} = 546.07\text{nm}$  (Ucsc, 2022). Next, we must account for  $m_j$  of these terms to apply our energy orientation equations.

$$\begin{aligned} ^3S_1 &\implies j_T = 1 \implies m_{j_T} = [-1, 0, 1] \\ ^3P_2 &\implies j_T = 2 \implies m_{j_T} = [-2, -1, 0, 1, 2] \end{aligned}$$

We apply our restrictions to reduce the 15 possible magnetic dipole transitions to 9. The electric dipole transition has  $\Delta\ell_T = 1$ , which agrees with our restrictions. While our magnetic dipole transitions have  $\Delta j_T = 1 \implies \Delta m_j = 0, \pm 1$ , and  $\Delta s_T = 0 \implies \Delta m_s = 0$ ; also in agreement. See **Figure. 3** for a rendition of all the mentioned transitions.

Next we show the energy calculation for the  $\Delta m_{j_T} = 0$  or  $\pi$  lines which can be extended to show the  $\Delta m_{j_T} = \pm 1$  or  $\sigma$  lines. First, using **Equation 3** we calculate  $g_{\text{Lande}}$  for each term.

Let  $^3S_1$  be represented with a subscript (+) and  $^3P_2$  with (-).

$$\begin{aligned} g_{L+} &= 1 + \frac{1(1+1) + 1(1+1) - 0(0+1)}{2(1)(1+1)} = 2 \\ g_{L-} &= 1 + \frac{2(2+1) + 1(1+1) - 1(1+1)}{2(2)(2+1)} = \frac{3}{2} \end{aligned}$$

Our magnetic dipole orientation energy is then,

$$\delta E = g_L \cdot m_j \cdot \mu_0 \cdot B_{\text{ext}} \begin{cases} 2 \cdot m_{j+} \cdot \mu_0 \cdot B_{\text{ext}} : & ^3S_1 \\ \frac{3}{2} \cdot m_{j-} \cdot \mu_0 \cdot B_{\text{ext}} : & ^3P_2 \end{cases} \quad (4)$$

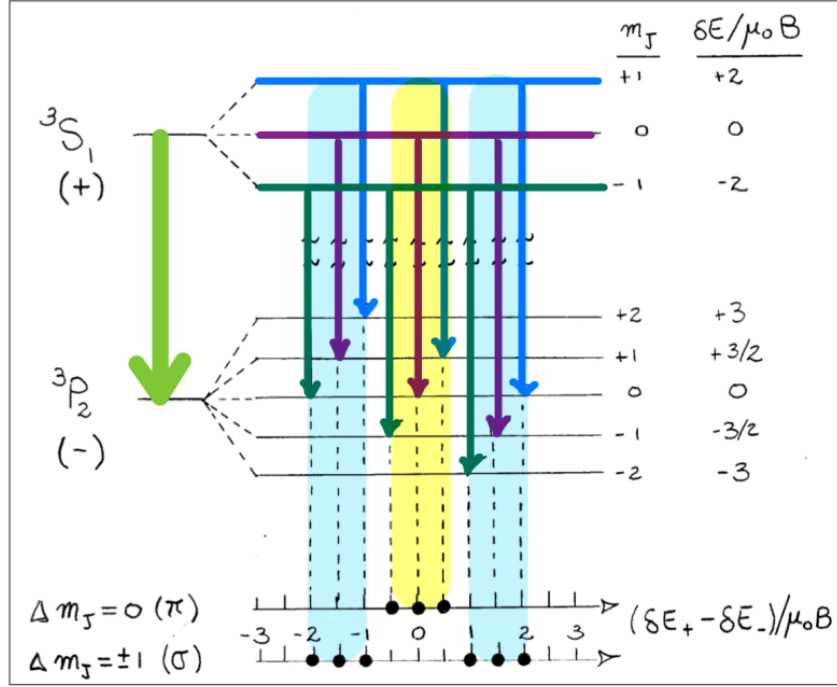


**Figure 3:** The energy levels for the  $^3S_1 \Rightarrow ^3P_2$  transition in mercury. The left-most green arrow is our electric dipole transition, while the 9 blue, green, and purple arrows are the magnetic dipole transitions. The 9 transitions are identified by their  $m_j$  value and their orientation energy  $\delta E$ . The restrictions categorize these transitions into  $\pi$  and  $\sigma$  lines. The x-axis represents the relative spacing between energies (Ucsc, 2022)

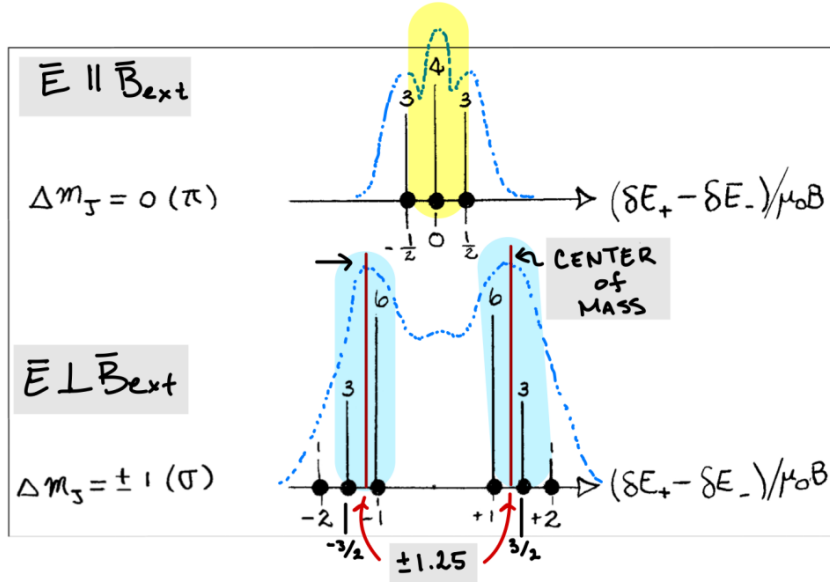


**Figure 4:** Relative intensities of the Zeeman lines. This is our theoretical model of what we expect to see in our data. The  $\pi$  lines (yellow) appear parallel to  $B_{ext}$  while the  $\sigma$  lines (blue) are perpendicular. The x-axis is the same as in Figure. 3. The  $\sigma$  lines will not resolve as they are too closely spaced, but the resulting peaks correlate to the line's center of mass (Ucsc, 2022).

Transition from (+)  $\longrightarrow$  (-),  $\Delta m_{j_T} = 0$  :

$\delta E_+$ :

$$\begin{aligned} m_{j_T} = 1 & \quad \delta E_+ = 2(1)\mu_0 B_{ext} \\ m_{j_T} = 0 & \quad \delta E_+ = 2(0)\mu_0 B_{ext} \\ m_{j_T} = -1 & \quad \delta E_+ = 2(-1)\mu_0 B_{ext} \end{aligned}$$

$\delta E_-$ :

$$\begin{aligned} m_{j_T} = 1 & \quad \delta E_- = \frac{3}{2}(1)\mu_0 B_{ext} \\ m_{j_T} = 0 & \quad \delta E_- = \frac{3}{2}(0)\mu_0 B_{ext} \\ m_{j_T} = -1 & \quad \delta E_- = \frac{3}{2}(-1)\mu_0 B_{ext} \end{aligned}$$

$$\Delta E_{m_i}^\pi = E_i \tag{5}$$

$$\Delta E_{m_i}^\pi = \delta E_+ - \delta E_- = E_i \quad \text{for } i \in [1, 2, 3] \quad \left\{ \begin{array}{l} E_1 = \Delta E_1^\pi = \frac{1}{2}\mu_0 B_{ext} \\ E_2 = \Delta E_0^\pi = 0 \\ E_3 = \Delta E_{-1}^\pi = -\frac{1}{2}\mu_0 B_{ext} \end{array} \right.$$

The values for  $\Delta E_{m_i}^\pi$  can be rewritten to reflect the x-axis of **Figure. 3** and **Figure. 4**. Indicating that the relative energy spacing between transition lines is 1/2. **Figure. 4** has blue dashed lines which provide a glimpse into our expected graphs. Note that the peaks of our  $\sigma$  lines will not resolve due to instrument limitations. However, the peaks viewed should represent our theoretical line intensities' center of mass (COM).

Calculation of COM position for the right  $\sigma$  peak, where  $m_i$  will be our relative intensities and  $x_i$  our positions on the x-axis.

$$\begin{aligned} \bar{x} &= \frac{m_1 x_1 + m_2 x_2 + m_3 x_3}{m_1 + m_2 + m_3} \\ &= \frac{6(1) + 3(\frac{3}{2}) + 1(2)}{6 + 3 + 1} \\ &= 1.25 \end{aligned}$$

Since the COM is at  $\pm 1.25$ , we can assume our dashed image is a reasonable prediction. We expect to see a gradual slope in the center and a steep slope off the sides. The intensity profiles will be fit to a graph of  $\Delta E_i$  vs.  $B_{ext}$  to measure  $\mu_0$ , hence, affirming the existence of intrinsic spin.

## 2 Methods

### 2.1 Apparatus

We will use a magnet and optical instruments to observe the splitting of mercury's strong-green line. **Figure .5** is an image of our physical setup. Our rays travel from left to right. A Mercury Geissler tube starts off the line placed strategically within the magnet. We pass an alternating current through the gas to induce excitation. In front of the tube is a small metal aperture. The aperture ensures light directly under the influence of the magnet is directed down to the optical setup.

Following the aperture, some distance away, is a condenser that collects as much light as possible to pass down the optical train. A filter is placed directly before the interferometer to ensure we only witness light within our target wavelength. Once the light enters the interferometer, it acts as a diffraction grating. The interferometer increases the resolution of our incoming rays and outputs a circular interference pattern. Next is our polarizer, which allows us to select specific polarized light affected by the magnetic field. In our experiment, we will have the polarizer in either a 90 degree or 180 degree position to observe the different splittings. After this, another slightly larger aperture from the one previously mentioned directly follows the polarizer. We reasoned this was an additional measure to keep out unwanted light.

Our final stop is the astronomical CCD camera which works off the premise of the photoelectric effect. The tiny microchip (CCD) is very good at detecting photons as they impede upon it, which converts to data, then an image is sent to our computer software, where it creates intensity profiles for analysis. Here we have more control over the exposure time and other nuances. However, I realized I had put too much effort into the theory and forgot to cover the software. The software is intentionally left out of the paper, but it is greatly missed. Lastly, we take sample images of the light with the magnet turned off for calibration and on to witness the splitting.

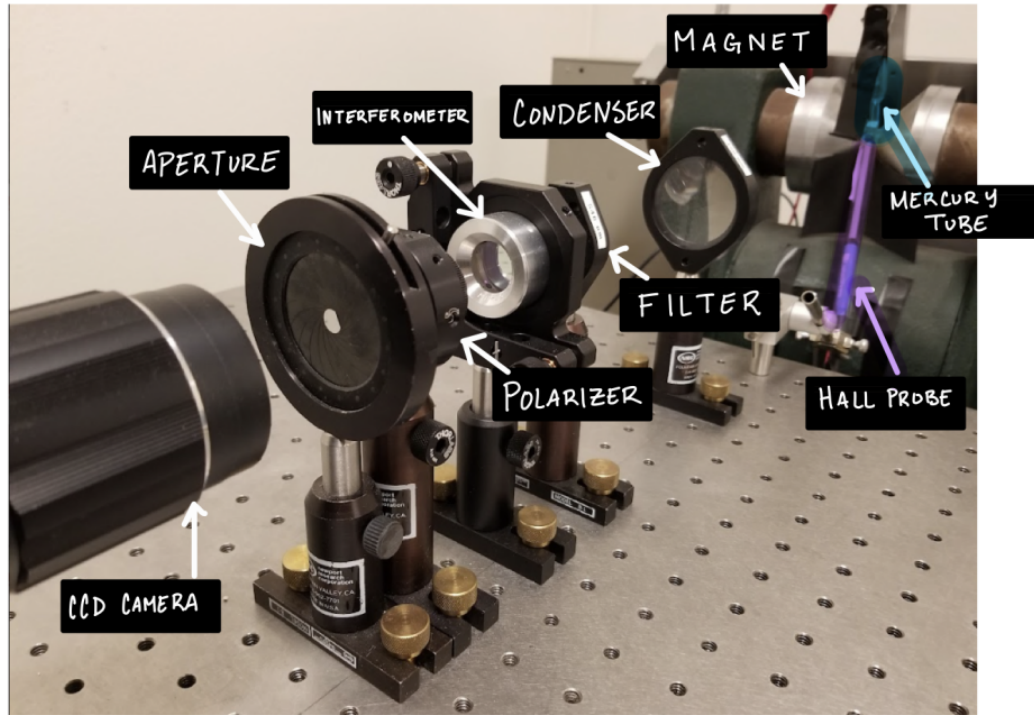


**Figure 5:** Image of the full optical line. Rays travel from left to right. Mercury Geissler Tube (blue highlight), Hall Probe (purple highlight), Horseshoe Magnet, Condenser, Filter, Interferometer, Polarizer, Aperture, and the CCD Camera. Images from the CCD camera are processed by its associated software where exposure time and other qualities are adjusted.

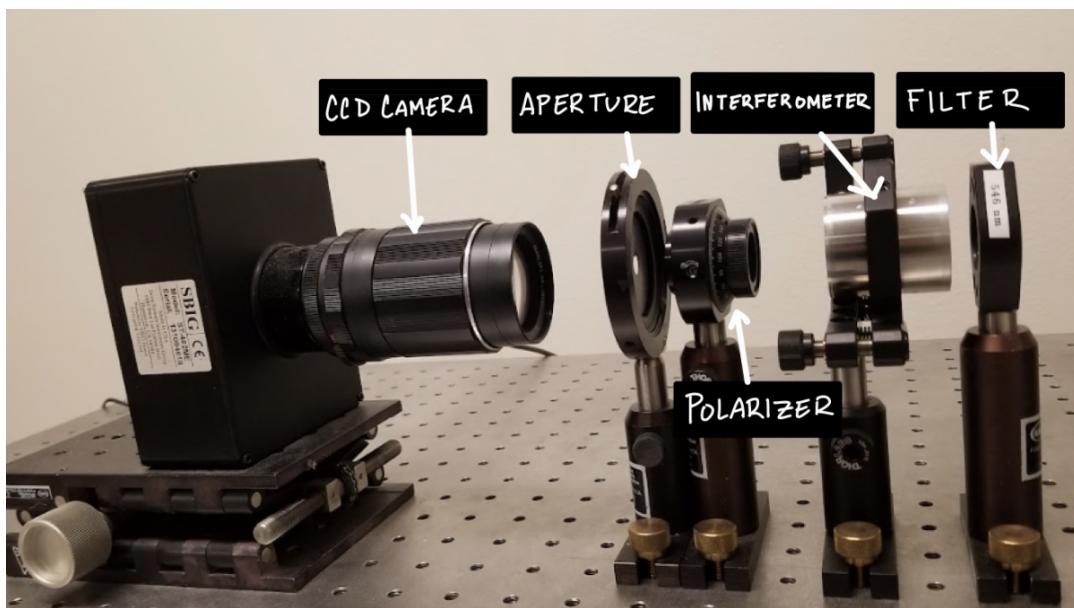


**Figure 6:** Image of optical setup taken from a different angle to better see the polarizer dial and camera. Rays incoming from left to right. Filter, Interferometer, Polarizer, Aperture, and the CCD Camera.



### 2.1.1 Mercury Light Source

Our light source is a hollow-cathode Mercury discharge Geissler tube. We used a step-down autotransformer to a step-up high voltage transformer to run the necessary current through the tube to cause excitation. We ran the autotransformer at 45V (Ucsc, 2022). During collection, the room is kept dark to reduce the interference from stray light, and several black pieces of paper were placed about the magnet to reduce the chance of reflection.

### 2.1.2 Magnetic Field

The Magnet is an iron-core electromagnetic arranged in a horseshoe configuration. A KEPCO, inc power supply is adjusted using the current limit knob while setting the voltage knob to maximum. A gaussmeter hall probe takes measurements in kilo Gauss (Ucsc, 2022). The hall probe is not placed directly on the sample rather it is placed just below, as seen in **Figure .5**.

### 2.1.3 Condenser

The Condenser, a bi-convex lens, collects as much light from the source and conveys to the rest of the optical elements.

### 2.1.4 Interference Filter

To study the target spectral line of mercury, we use the filter to remove all other lines of the spectrum using the interference filter. The spectral response is between 540-550 nm with a little over 60% peak transmission, about 545nm, with tails at 10% transmission. Well within our target value (Ucsc, 2022).

### 2.1.5 Polarizer

The polarization theory is the only theory that escaped me. As noted in the 134 UCSC Manual (2022),

*“if our line of sight to the source is perpendicular to the magnetic field direction, the polarization of the light has the following property: light emitted from the three  $\Delta m_j = 0$  transitions will be polarized parallel to the magnetic field. Conversely, light emitted from the 6  $\Delta m_j = \pm 1$  transitions will be polarized perpendicular to the magnetic field.”*

I reasoned this was because of the relation,

$$\vec{B} \propto \vec{v} \times \vec{E}$$

Where  $\vec{B}$  is our magnetic field,  $\vec{v}$  is the velocity of the electron, and  $\vec{E}$  represents our light. However, this is the extent to which I could find a definitive answer. Most of the effort was directed

to the quantum mechanical aspects of this experiment. (sorry)

### 2.1.6 Fabry-Perot Interferometer

This instrument is a high-resolution interferometer. It comprises two optical flats separated by a hollow spacer of width  $t = 0.6499\text{cm}$ . This width is given in the UCSC (2022) manual and not measured. The flats are coated with a reflective layer which gives a reflection of about 90% (Ucsc, 2022). The interferometer takes incoming light and outputs a series of concentric rings with order ( $p = 1, 2, 3, \dots$ ). These rings are imaged onto our camera's lens by focusing them at infinity. Their angular size is given by,

$$\theta_p^2 = \frac{\lambda}{t}(p - e(\lambda)) \quad p = 1, 2, 3, \dots \quad (6)$$

Where  $\lambda$  will be our examined line and  $e(\lambda)$  is a constant arising from  $t$  not being an integer multiple of  $\lambda$ . However, it serves no purpose in our experiment, as we will see in the following equation.

Our experiment will observe the finely spacing "splitting" of our target wavelength. The result is two closely spaced lines,  $\lambda_1$  and  $\lambda_2$  as a result of their discrete polar angles,  $\theta_1^{(p)}$  and  $\theta_2^{(p)}$ . For a fixed ring  $p = 1$ , their displacement is represented as,

$$(\theta_1)^2 - (\theta_2)^2 \simeq 2\bar{\lambda} \left( \frac{1}{\lambda_1} - \frac{1}{\lambda_2} \right) \simeq \frac{2}{\bar{E}} \cdot (E_1 - E_2) = \frac{2}{\bar{E}} \cdot (A\mu_0 B_{ext}) \quad (7)$$

Where  $\bar{E} = 3.638 \cdot 10^{-12}$  erg is the energy that correlates to  $\bar{\lambda}$ . The left most equation shows the replacement of,

$$\boxed{\Delta E_i = E_1 - E_2 = A\mu_0 B_{ext}} \quad (8)$$

from **Equation 5**. Where  $A$  is the separation constant we determine from measurement. **Equations 6 & 7** are derived in the Appendix of the UCSC Manual (2022). Notice how the constant  $e(\lambda)$  does not appear in **Equation 6**, this is because we are interested in the difference and each line will contain the same constant value.

The FWHM equation gives the resolving power of our interferometer,

$$\frac{\Delta\lambda}{\lambda} = \frac{\lambda}{2t} \frac{1 - R}{\pi\sqrt{R}} \quad (9)$$

For our values and a reflection coefficient of  $R \approx 0.9$ , we get  $\text{FWHM} = 1.4 \cdot 10^{-6}$  meaning if our peaks are more than this value in separation, we should be able to resolve them.

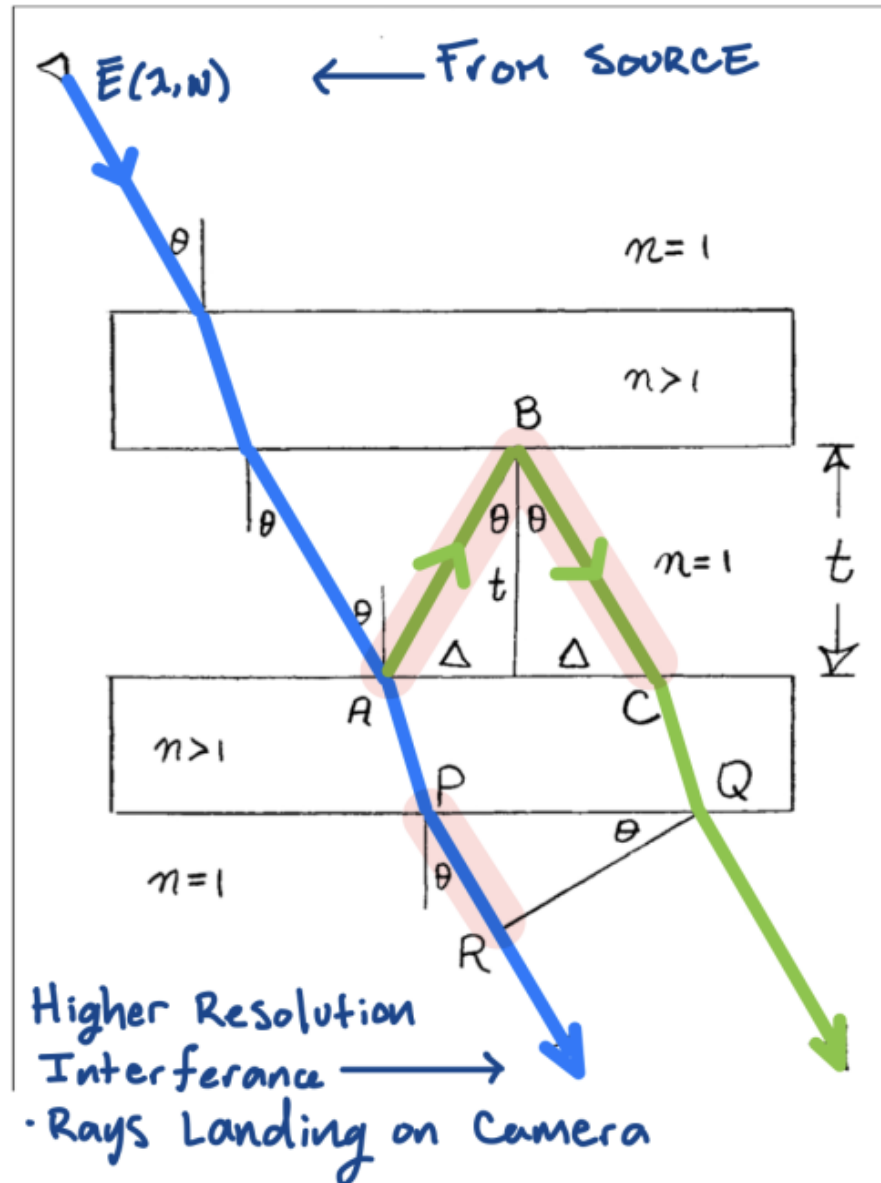


**Figure 7:** Ray diagram of the Fabry-Perot Interferometer. Top: Rays are incoming from the source light and reflected within the two flats. The reflected ray is green, and it branches away from the blue ray. The red highlighted portion is the extra distance taken by the green ray, which needs to be an integer multiple of the wavelength of our incoming ray to interfere constructively. More on this is found in the Appendix (Ucsc, 2022)

### 2.1.7 Astronomical CCD Camera

A CCD is a tiny microchip which stands for Charged Coupled Devices and are sensitive detectors of photons typically used in telescopes. They measure light by taking advantage of the photoelectric effect. They measure the number of electrons released from each pixel after collision by a photon. Our Camera should be focused at infinity to obtain the sharpest rings and satisfy the interferometer equations. The camera has an array of 510x765 pixels, each 9 $\mu$ m x9 $\mu$ m square.

Using **Figure. 8** we can derive an equation from the Thin Lens Formula to obtain  $\theta$  values from **Equation 7**.

$$\begin{aligned}\frac{1}{f} &= \frac{1}{S_{obj}} + \frac{1}{S_i} \\ \frac{1}{f} &= \frac{1}{\infty} + \frac{1}{S_i} \\ \frac{1}{f} &= \frac{1}{S_i} \implies f = S_i\end{aligned}$$

Where  $f = 135\text{mm}$  is our cameras focal length,  $S_i$  is the image distance, and  $S_{obj}$  is the objects distance. Setting the camera to focus at infinity implies we set the object distance to infinity. Next, we make a small angle approximation and use the geometry of our set up to define an equation for  $\theta$  as a function of our measured radius ( $r$ ).

$$\tan \theta = \frac{r}{f} \quad \text{where } \tan \theta \approx \theta \implies \theta \approx \frac{r}{f} \quad (10)$$

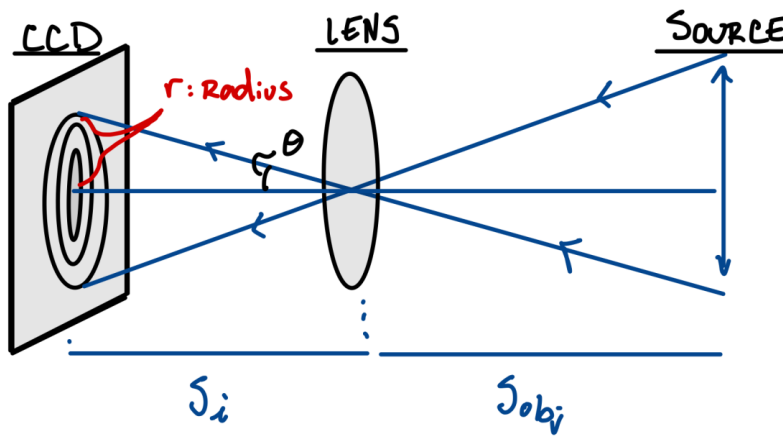


**Figure 8:** An oversimplified ray diagram of our CCD Camera. Rays are incoming from right to left at a field dimension angle  $\theta$ . The lens is set to focus at infinity to produce the sharpest rings (Ucsc, 2022).

## 2.2 Measurement

This section presents the equations and the methods used in taking a measurement. The only measurements taken will be from our intensity profiles and the Hall Probe. The profiles are processed using python code to extract energy shift values. Magnetic field values are measured with uncertainties at the moment of capture and assigned to each profile. Selecting peaks is the same across all measurements. We used `scipy.signal`'s `find_peaks` function to find the pixel location associated with each unique peak.

### 2.2.1 Calibration Calculation

We collect an intensity profile with the magnetic field turned off to calibrate. However, our Hall probe was still measuring a value with the magnet turned off. This was unaccounted for in our results, as in we did not tare our values from this residual magnetic field. **Figure. 9** is the physical image of our interference pattern and **Figure. 10** is its intensity profile. The intensity values are in ADU, and our x-axis is the pixel location.

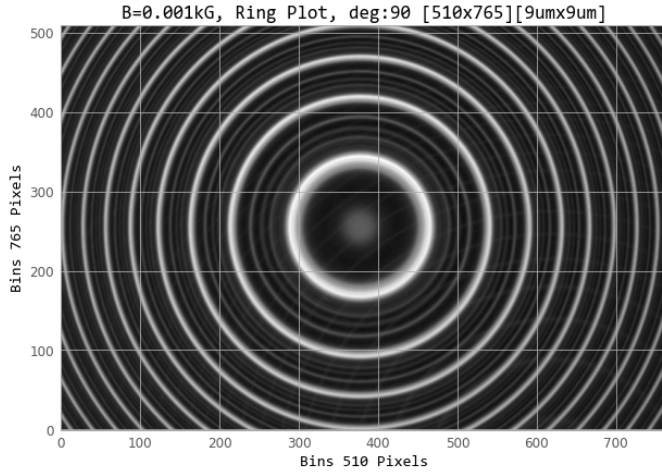


**Figure 9:** Image taken from CCD of Mercury's interference pattern. The bright/thick center ring is an example of  $p=1$ . Faint white rings appear to crossover Mercury's rings that were not accounted for in the results.

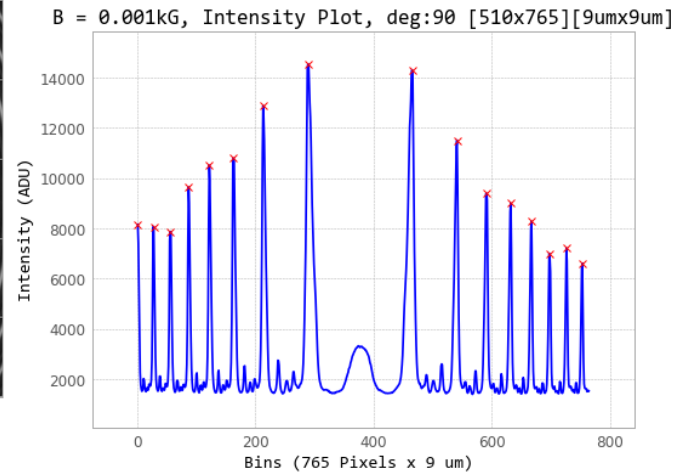


**Figure 10:** Intensity profile of  $B_{ext} = 0.001\text{kG}$ . The large vertical lines correlate to the cross-section of bright white rings of Figure. 9.

To calibrate we first select our peaks as seen by red (x) in **Figure .10**. Diameter values are calculated from the pixel locations. We have 16 visible peaks correlating to 8 rings. The following is a simple radius calculation and use of **Equation 10**.

$$D_i = x_a - x_b \quad (11)$$

$$r_i = D_i/2 \quad (12)$$

$$\theta_i = \frac{r_i}{f} \quad (13)$$

Where the subscript  $i$  specifies each ring and  $D$  is the diameter. Next we plot and fit  $\theta^2$  values vs. their respective index in **Figure 11**. Using scipy.optimize's curve\_fit function we fit  $\theta^2$  and  $p$  to **Equation 6**.

$$\theta_p^2 = \frac{\lambda}{t}(p - e(\lambda)) \quad p = 1, 2, 3, \dots$$

Where we fixed  $t = 0.6499\text{cm}$  and found best fit parameters for  $\lambda = \bar{\lambda}$  and  $e(\lambda)$ .

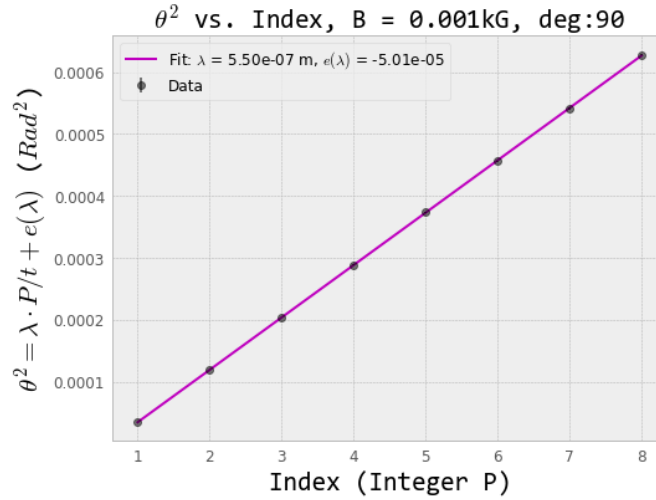


**Figure 11:** Fit graph for calibration Equation 6. The polarizer was set to 90 degrees during collection. The magnetic field was not zero even though the magnet was turned off 0.001kG was the reading. The calibration was a success with a p-value = .78

With a percent error less than 1% and a p-value = .78 > 0.05 indicating our fit is within reason we choose to continue with our analysis. See the Appendix for **Table .5** for a comprehensive list of statistical values.

### 2.2.2 Energy Shift Calculation

To aid analysis we included **Figure. 12** which is an example of our intensity profiles based on **Figure. 4**.

Similar to our calibration, we use the `scipy.signal` package to obtain our peak pixel value and calculate  $\theta$ . However, since **Equation 7** depends on  $\bar{E}$  we must select peaks located about this value.  $\bar{E}$  represents not only our main energy line but the average value of the splitting. This is shown in **Figure. 12** with a green highlight. The figure also identifies how we selected our peaks and determined our radius values.

We used only the  $p = 1$  (center) ring for each profile. 11 trials were done for  $\pi$  and 10 for  $\sigma$ .

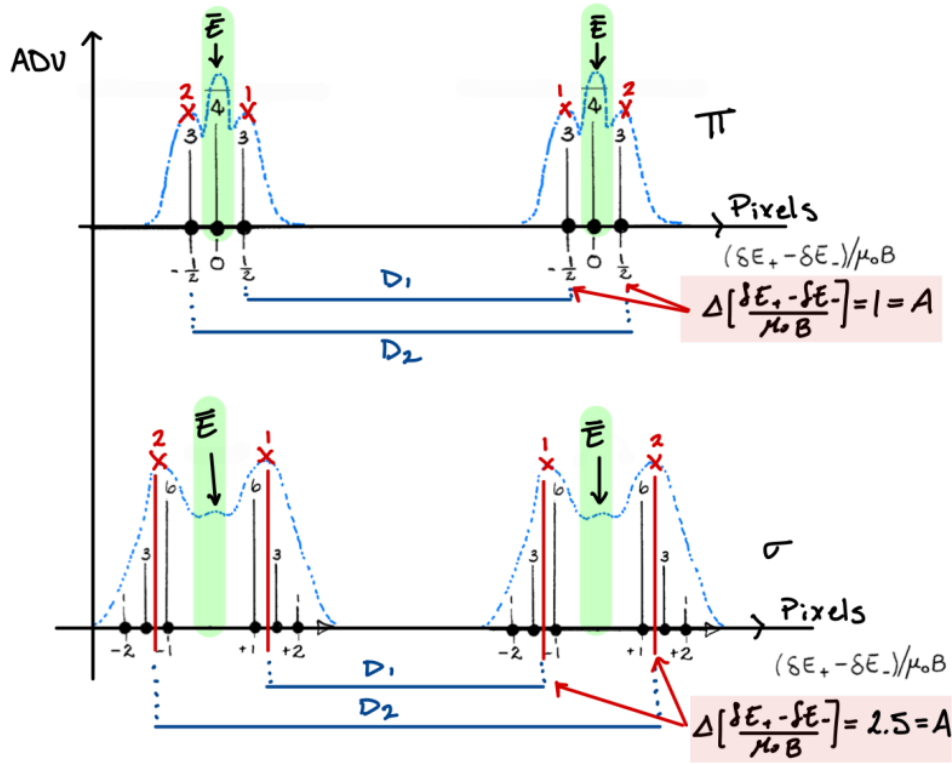


**Figure 12:** Peak selection from intensity profiles [ADU vs. Pixel]. Top:  $\pi$  profile with  $p = 1$  ring. Peaks are selected about the central line, labeled with red (x)'s. Bottom:  $\sigma$  profile with  $p = 1$  ring. Peaks were also selected about the central line. Values  $D_1$  and  $D_2$  are the diameters of the respective rings. The relative difference in our selected peaks is labeled with  $A$  (Ucsc, 2022)

Calculations from measured pixel values  $(x_1, x_2)$ :

Convert to meter and obtain  $\theta$ :

$$x_i = x_i \cdot (9 \cdot 10^{-6})$$

$$D_i = x_1 - x_2$$

$$r_i = D_i/2$$

$$\theta_i = \frac{r_i}{f}$$

Each profile will contribute two  $\theta$  values therefore 1  $\Delta E_i$  value (**Equation 8**),

$$\Delta E_i = \frac{\bar{E}}{2} \left( (\theta_1)^2 - (\theta_2)^2 \right) \quad (14)$$

These  $\Delta E_i$  values are then plot and fit against their associated  $B_{ext}$  values.

### 2.2.3 Bohr Magnetron $\mu_0$ Calculation

Our fitted values for  $\Delta E_i$  do not take into account any error from our magnetic field. To compensate for this, we take the  $\Delta E_i$  values,  $B_{ext}$  values, and their uncertainties and propagate them into  $\mu_0$ . This is done for both  $\pi$  and  $\sigma$  lines.

Using **Equation 8** we can rewrite it to get  $\mu_0$ ,

$$\mu_{0i} = \frac{\Delta E_i}{A \cdot B_{ext-i}} \quad (15)$$

With each set of  $\mu_{0i}$  a weighted average can be done.

Equations:

$$\bar{\mu} = \frac{\sum_i^n \left( \frac{\mu_i}{\sigma_{\mu_i}^2} \right)}{\sum_i^n \left( \frac{1}{\sigma_{\mu_i}^2} \right)} \quad (16)$$

$$\sigma_{\mu}^2 = \frac{1}{\sum_i^n \left( \frac{1}{\sigma_{\mu_i}^2} \right)} \quad (17)$$



## 2.3 Data and Uncertainty Analysis

The peaks were given an error of  $\pm 2$  pixels for narrow peaks and  $\pm 3.5$  pixels for broader peaks. Our Results section contain images that reflect this decision. The magnetic field was given an error of  $\pm 0.05\text{kG}$  based on the instrumentation. However, we did not incorporate other errors that occurred from the placement of the probe.

### 2.3.1 Calculation of Uncertainties

The following are equations used to propagate the error from our pixel selection to  $\Delta E_i$ .

$$\sigma_D^2 = (\sigma_{x_f})^2 + (\sigma_{x_i})^2 \quad (18)$$

$$\sigma_r^2 = \left(\frac{1}{2}(\sigma_D)\right)^2 \quad (19)$$

$$\sigma_\theta^2 = \left(\frac{1}{f}\right)^2 (\sigma_r)^2 \quad (20)$$

$$\sigma_{\Delta E_i}^2 = (\bar{E} \cdot \theta_1)^2 (\sigma_{\theta_1})^2 + (\bar{E} \cdot \theta_2)^2 (\sigma_{\theta_2})^2 \quad (21)$$

The following equation is used to propagate the error from  $\Delta E_i$  and  $B_{ext}$  to  $\mu_0$ .

$$\sigma_{\mu_{0i}}^2 = \left(\frac{1}{A \cdot B_{ext-i}}\right)^2 (\sigma_{\Delta E_i})^2 + \left(\frac{\Delta E_i}{A \cdot B_{ext-i}^2}\right)^2 (\sigma_{B_{ext-i}})^2 \quad (22)$$

Lastly, the following equation is used in the propagation of error from our calibration. This depends on the propagation **Equations (18 - 20)**.

$$\sigma_{\theta^2} = (2\theta)(\sigma_{\theta}) \quad (23)$$

### 2.3.2 Hypothesis Testing

Based on reasoning outlined in **Figure.12** we assume the constraint A on each fitted graph in our results section. Based on the electron spin theory, which provided our relative spacing, we assume that our  $\pi$  lines will give a slope of  $A\mu_0$  such that  $A = 1$ , while our  $\sigma$  lines give a constant of  $A = 2.5$ .

### 3 Results

The following three graphs show the splitting of Mercury's green strong line. Each graph shows the  $p = 1$  ring, represented in their relative pixel positions—the  $\sigma$  lines resolved at relatively low magnetic field values. As reflected in the graph titles, the  $\pi$  lines required more strength to resolve fully.

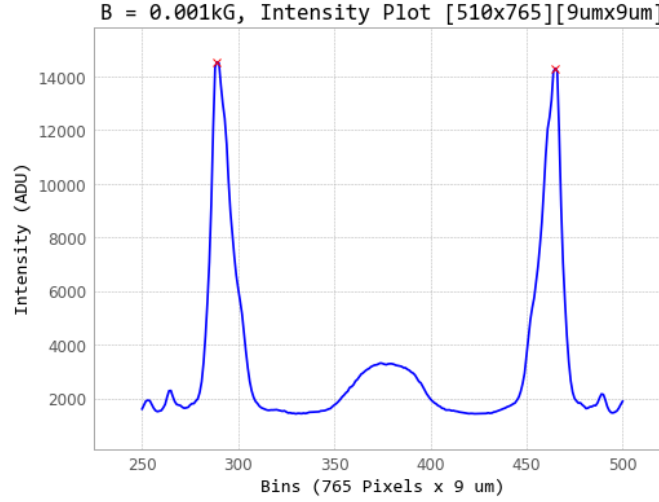


**Figure 13:** Mercury's  $p=1$  ring intensity profile. This graph is a truncated version of Figure .10. Note that the ring values are located approximately at pixel values 290 and 460.

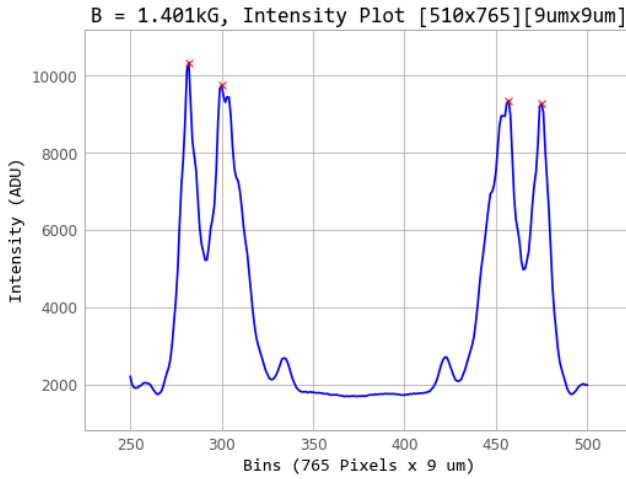


**Figure 14:**  $\sigma$  line splitting observed at  $B = 1.401\text{kG}$ . The relative locations of the peaks are similar to Figure .13. The peaks are not fine points and attribute error of  $\pm 2$  pixels for narrower peaks and  $\pm 3.5$  pixels for wider ones.

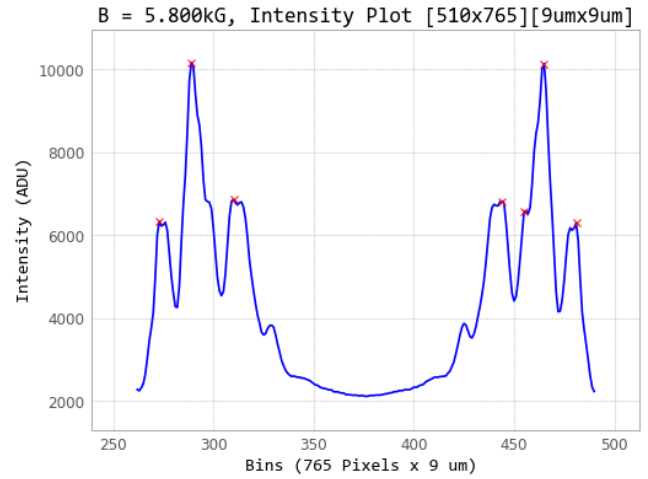


**Figure 15:**  $\pi$  line splitting observed at  $B = 5.800\text{kG}$ . The relative locations of the peaks are similar to Figure .13. The peaks are not fine points and attribute error of  $\pm 2$  pixels for narrower peaks and  $\pm 3.5$  pixels for wider ones.

### 3.1 $\sigma$ Lines

The fit equation:

$$\Delta E_i = A\mu_0 B_{ext} \quad \text{for } A = 2.5$$

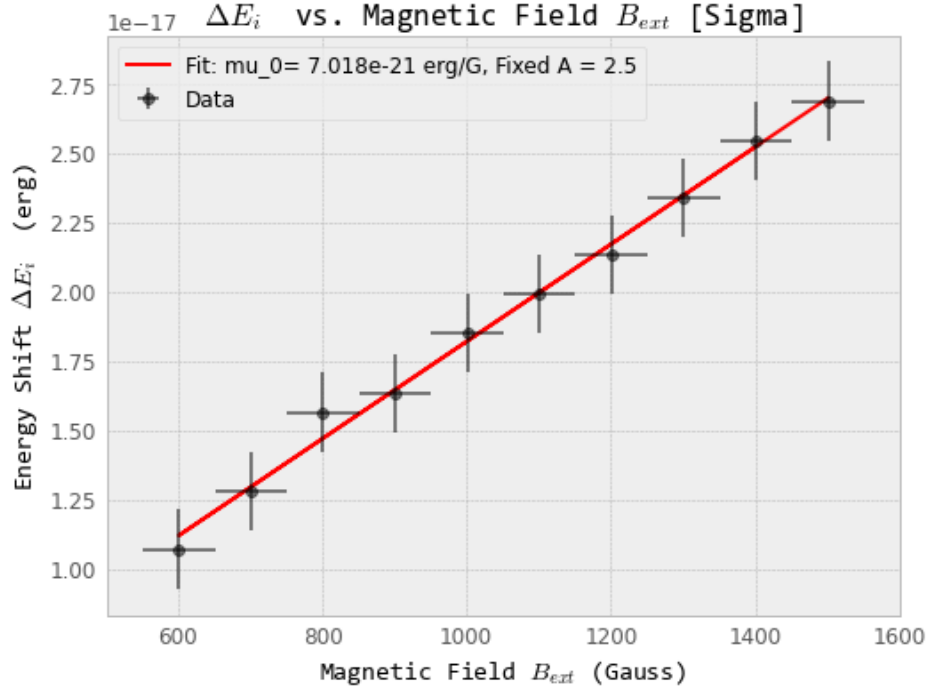


**Figure 16:** Fit Graph for  $\sigma$  lines taken at 180 degrees. The fitting function is shown above the graph with the value  $A = 2.5$  fixed. The best fit values are shown on the plot and in Table 1.

**Table 1:** Fitted Values from  $\sigma$  Trials.

Item	Value	Uncertainty	Unit
True $\mu_0$	9.27E-21		erg/Gauss
<b>Fit Values</b>			
Mu	7.02E-21	6.28E-22	erg/Gauss
<b>Stats</b>			
$\chi^2$	0.73		
Degrees of Freedom	8		
Reduced $\chi^2$	0.09		
CDF	0.0005		
p-value	.99		

## 3.2 $\pi$ Lines

The fit equation:

$$\Delta E_i = A\mu_0 B_{ext} \quad \text{for } A = 1$$

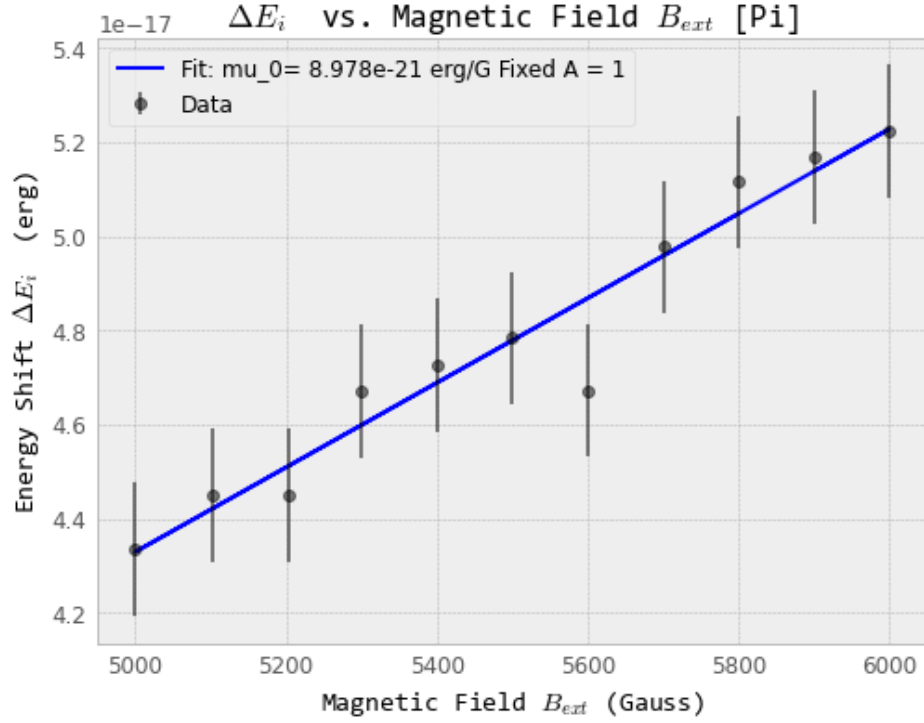


**Figure 17:** Fit Graph for  $\pi$  lines taken at 90 degrees. The fitting function is shown above the graph with the value  $A = 1$  fixed. The best fit values are shown on the plot and in Table 2

**Table 2:** Fitted Values from  $\pi$  Trials.

Item	Value	Uncertainty	Unit
True $\mu_0$	9.27E-21		erg/Gauss
<b>Fit Values</b>			
Mu	8.98E-21	1.35E-21	erg/Gauss
<b>Stats</b>			
$\chi^2$	2.82		
Degrees of Freedom	9		
Reduced $\tilde{\chi}^2$	0.31		
CDF	0.028		
p-value	0.97		

### 3.3 $\mu_0$

Using the calculations from Equations 15, 22, 16, and 17 we obtained two  $\mu_0$  values each specific to either  $\sigma$  or  $\pi$ . Our  $\sigma$  lines gave  $\bar{\mu}_0 = (8.689 \cdot 10^{-21} \pm 8.091 \cdot 10^{-23})$  erg/Gauss and our  $\pi$  lines gave  $\bar{\mu}_0 = (7.250 \cdot 10^{-21} \pm 1.960 \cdot 10^{-22})$  erg/Gauss. These results proved consistent with the expected value  $\mu_0 = 9.2741 \cdot 10^{-21}$  erg/Gauss with respective statistical values ( $\chi^2$   $p = .97$ ) and ( $\chi^2$   $p = .99$ ).

## 4 Discussion

In both  $\pi$  and  $\sigma$  trials we measured  $\mu_0$  to be in agreement with the established value  $\mu_0 = 9.2741 \cdot 10^{-21}$ . The significance of measuring  $\mu_0$  was to confirm the existence of the intrinsic quantum number spin. Specifically, to show the theory that electrons with half integer spin are constrained to angular momentum conservation rules related to the photon's spin 1 value. By finding our values agree with the established value we can confidently say the experiment was a success.

However several factors could be improved and we should address areas of uncertainty which were not account for in analysis. A major contribution to error is the measure of the magnetic field. Since we are unable to measure the field exactly in the location of the mercury tube the values we measured are affected by the relative distance. A possible solution would be calibrate the placement of our hall probe. A formula for B vs distance could be determined and interpolated to determine the magnetic field at the source. Another option would be a magnet that clearly states the magnetic field as it's produced, but that may be more expensive.

Another source of error may lie in the interferometer's inability to resolve all the theoretical lines. For instance, our  $\sigma$  lines depend on the center of mass calculation, but other isotopes could be appearing in our data which weight the locations of COM in different directions. Besides increasing resolution another fix was not considered.

In future trails a larger data set would also be beneficial. This experiments was reduced to 2 trials of about 10 data points because the first two attempts made to measure the peaks resulted in inconclusive data. We discovered the focus was not set to infinity and the range of magnetic field values were not producing anything for our  $\pi$  lines. We discovered the  $\pi$  lines require higher field strength to split. Our reasoning is because the these lines are centered about the main line low field strength mixed with our resolution limitation are unable to resolve them.

## 5 Appendix

### 5.1 Data Tables

**Table 3:** Table of  $\Delta E_i$  and  $B$  values for both  $\sigma$  and  $\pi$  lines. Values are taken from  $p = 1$  rings. Values are calculated from our measured diameters and the uncertainty from our peak pixel selection is propagated with an average error of  $\pm 2.75$  pixels.

$\sigma$		$\pi$	
$\Delta E_i$ (erg)	B (Gauss)	$\Delta E_i$ (erg)	B (Gauss)
2.69E-17	1501	5.17E-17	5900
1.07E-17	601	5.22E-17	6000
1.28E-17	701	4.34E-17	5000
1.57E-17	801	4.45E-17	5103
1.63E-17	901	4.45E-17	5203
1.85E-17	1001	4.67E-17	5299
1.99E-17	1101	4.73E-17	5400
2.13E-17	1201	4.78E-17	5500
2.34E-17	1301	4.67E-17	5600
2.55E-17	1401	4.98E-17	5700
		5.11E-17	5800

**Table 4:** Table of  $\mu_0$  and  $\sigma_{\mu_0}$  values for both  $\sigma$  and  $\pi$  lines. Their weighted averaged values are  $(8.689 \cdot 10^{-21} \pm 8.091 \cdot 10^{-23})$  and  $(7.250 \cdot 10^{-21} \pm 1.960 \cdot 10^{-22})$  respectively. Equation to reference: Equation 15 found in section 2.2.3.

$\sigma$		$\pi$	
$\mu_0$	$\sigma_{\mu_0}$	$\mu_0$	$\sigma_{\mu_0}$
7.16E-21	4.48E-22	8.76E-21	2.50E-22
7.12E-21	1.12E-21	8.70E-21	2.46E-22
7.31E-21	9.66E-22	8.67E-21	2.97E-22
7.82E-21	8.63E-22	8.72E-21	2.90E-22
7.24E-21	7.48E-22	8.55E-21	2.84E-22
7.39E-21	6.79E-22	8.82E-21	2.81E-22
7.24E-21	6.14E-22	8.75E-21	2.75E-22
7.11E-21	5.60E-22	8.70E-21	2.69E-22
7.20E-21	5.18E-22	8.34E-21	2.61E-22
7.27E-21	4.82E-22	8.73E-21	2.59E-22
		8.82E-21	2.55E-22

**Table 5:** Fitted values for our calibration test using Equation 6.

Item	Value	Uncertainty	Unit
True $\lambda$	5.4607		nm
<b>Fit Values</b>			
$\lambda$	5.50E-07	$\pm 8.81\text{E-}10$	m
$e(\lambda)$	-5.01E-05	$\pm 4.12\text{E-}07$	m
<b>Statistical Values</b>			
$\chi^2$	3.22		
Degrees of Freedom	6		
Reduced $\chi^2$	0.53		
CDF	0.22		
p-value	.78		

## References

- [1] A J Kox. (1997) The Discovery of the electron: II. The Zeeman effect. *European Journal of Physics* 18 139.
- [2] Bosch, W.Gordy et al.(1957) The Zeeman Effect. *Spektroskopie II/Spectroscopy II*, 296-297.
- [3] Harris, R., 2014. *Modern physics*. Harlow: Pearson.
- [4] Perepelitsa D.V., (2007) Zeeman Effect in Mercury. *MIT Department of Physics*
- [5] U.C Santa Cruz. (2022) *Advanced Physics Laboratory*
- [6] Zeeman, P. (1902). *The Nobel prize in physics 1902*. NobelPrize.org. Retrieved June 5, 2022, from <https://www.nobelprize.org/prizes/physics/1902/zeeman/lecture/>